

- Natl. Acad. Sci. U.S.A.* **83**, 649 (1986); J.-K. Hwang, G. King, S. Greighton, A. Warshel, *J. Am. Chem. Soc.* **110**, 5297 (1988); B. Waszkowycz, I. H. Hillier, N. Gensmantel, D. W. Payling, *J. Chem. Soc. Perkin Trans. 2* **1991**, 225 (1991); P. A. Bash *et al.*, *Biochemistry* **30**, 5826 (1991).
15. P. A. Bash, M. J. Field, M. Karplus, *J. Am. Chem. Soc.* **109**, 8192 (1987).
  16. F. Floris and J. Tomasi, *J. Comput. Chem.* **10**, 616 (1989). The Lennard-Jones term accounts for the solute-solvent dispersion interaction that was neglected by the off-diagonal elements in the density matrix. In the present study, the following parameters were adopted ( $\sigma$  in angstroms,  $\epsilon$  in kilocalories per mole): C (3.50, 0.08); H (on C: 2.00, 0.01); H (on heteroatoms: 0.80, 0.10); O ( $sp^2$ : 2.95, 0.20); O ( $sp^3$ : 2.10, 0.15); O (water: 2.60, 0.15); N (2.50, 0.14); N (in NH and NH<sub>2</sub>: 2.80, 0.15); N (in ammonium ions: 3.10, 0.16).
  17. An effective potential was adopted for the solvent here. This is particularly advantageous in the present study over a polarizable potential such as the polarizable dipole model used by Warshel and co-workers (10) because the solute polarization properties, which are of the primary interest, can specifically be evaluated and decomposed. In addition, the TIP3P potential can also provide an excellent representation of the bulk structure and energy. An effective solvent potential as used here implies that the solvent polarization is already self-consistent, whereas the difference in the bulk and near the solute is negligible. Analogously, a uniform dielectric constant for the solvent has been widely used in continuum models including the work by Honig and co-workers (2). Remarkable agreement with experiment for ionic solvation has been obtained (2).
  18. C. J. F. Bottcher, *Theory of Electric Polarization* (Elsevier, Amsterdam, 1973).
  19. J. A. Pople and D. L. Beveridge, *Approximate Molecular Orbital Theory* (McGraw-Hill, New York, 1970); W. J. Hehre, L. Radom, P. v. R. Schleyer, J. A. Pople, *Ab Initio Molecular Orbital Theory* (Wiley, New York, 1986).
  20. W. L. Jorgensen, J. Chandrasekhar, J. D. Madura, R. W. Impey, M. L. Klein, *J. Chem. Phys.* **79**, 926 (1983).
  21. W. L. Jorgensen, *BOSS, Version 3.0* (Department of Chemistry, Yale University, New Haven, CT, 1991); J. Gao, *MCQUB* (Monte Carlo QM-MM at University at Buffalo, Department of Chemistry, State University of New York, Buffalo, 1992).
  22. M. J. S. Dewar, E. G. Zoebisch, E. F. Healy, J. J. P. Stewart, *J. Am. Chem. Soc.* **107**, 3902 (1985); M. J. S. Dewar, E. F. Healy, A. J. Holder, Y. C. Yuan, *J. Comput. Chem.* **11**, 541 (1990); J. J. P. Stewart, *ibid.*, p. 543.
  23. J. J. P. Stewart, *MOPAC*, Version 5 [Quantum Chemistry Program Exchange **6** (no. 391), 455 (1986)].
  24. R. W. Zwanzig, *J. Chem. Phys.* **22**, 1420 (1954).
  25. D. L. Beveridge and F. M. DiCapua, *Annu. Rev. Biophys. Chem.* **18**, 431 (1989); W. L. Jorgensen, *Acc. Chem. Res.* **22**, 184 (1989); P. A. Kollman and K. M. Mertz, *ibid.* **23**, 246 (1990).
  26. R. Wolfenden, L. Andersson, P. M. Cullis, C. C. B. Southgate, *Biochemistry* **20**, 849 (1981); A. Ben-Naim and Y. Marcus, *J. Chem. Phys.* **81**, 2016 (1984); R. G. Pearson, *J. Am. Chem. Soc.* **108**, 6109 (1986).
  27. J. A. Piccirilli, T. Krauch, S. E. Moroney, S. A. Benner, *Nature* **343**, 33 (1990); M. Perutz, *Mechanisms of Cooperativity and Allosteric Regulation in Proteins* (Cambridge Univ. Press, Cambridge, 1990); J. Gao, K. Kuczera, B. Tidor, M. Karplus, *Science* **244**, 1069 (1989); T. J. Murray and S. C. Zimmerman, *J. Am. Chem. Soc.* **114**, 4010 (1992).
  28. C. P. Smyth, *Dielectric Behavior and Structure: Dielectric Constant and Loss, Dipole Moment and Molecular Structure* (McGraw-Hill, New York, 1955).
  29. J. G. Kirkwood, *J. Chem. Phys.* **2**, 351 (1934); L. Onsager, *J. Am. Chem. Soc.* **58**, 1486 (1936); W. C. Still, A. Tempozak, R. C. Hawley, T. Hendrickson, *ibid.* **112**, 6127 (1990).
  30. C. J. Cramer and D. G. Truhlar, *Science* **256**, 213 (1992); *J. Am. Chem. Soc.* **113**, 8305 (1991); *ibid.*, p. 8552.
  31. M. W. Wong, M. J. Frisch, K. B. Wiberg, *J. Am. Chem. Soc.* **113**, 4776 (1991).
  32. D. Ceperley and B. Alder, *Science* **231**, 555 (1986); C. Zheng, C. F. Wong, J. A. McCammon, P. G. Wolynes, *Nature* **334**, 726 (1988).
  33. We thank B. R. Brooks, M. J. Field, H. F. King, R. W. Pastor, and D. G. Truhlar for comments on this work. This work has been stimulated by conversations with M. Karplus who posed the question of the significance of quantitative polarization contributions to the total electrostatic energy. The Petroleum Research Fund, administered by the American Chemical Society, the NIH (Biomedical Research Support Grants), and the State University of New York (SUNY) at Buffalo provided support for this research. The calculations were done on a SUN SparcStation 2 and a Titan 3000 at SUNY at Buffalo.

3 June 1992; accepted 11 August 1992

## Mercury Radar Imaging: Evidence for Polar Ice

Martin A. Slade,\* Bryan J. Butler, Duane O. Muhleman

The first unambiguous full-disk radar mapping of Mercury at 3.5-centimeter wavelength, with the Goldstone 70-meter antenna transmitting and 26 antennas of the Very Large Array receiving, has provided evidence for the presence of polar ice. The radar experiments, conducted on 8 and 23 August 1991, were designed to image the half of Mercury not photographed by Mariner 10. The orbital geometry allowed viewing beyond the north pole of Mercury; a highly reflective region was clearly visible on the north pole during both experiments. This polar region has areas in which the circular polarization ratio ( $\mu_c$ ) was 1.0 to 1.4; values  $< -0.1$  are typical for terrestrial planets. Such high values of  $\mu_c$  have hitherto been observed in radar observations only from icy regions of Mars and icy outer planet satellites.

Icy surfaces are common in the solar system, particularly on the moons of Jupiter and the rest of the outer planets. However, we were surprised to find that ice could exist on Mercury, the planet nearest the sun. Temperatures on Mercury reach as high as 700 K on the equator. Nevertheless, we interpret that a highly radar-reflective region observed on the north pole of Mercury in August 1991 is due to ices. The existence of the bright north polar feature was quickly confirmed at Arecibo, and a compact feature near the south pole was also discovered (1). We find that ices can be stable at the poles of Mercury over billions of years (2) owing to the temperature regimes (3) there. In this report, we present the observations that lead to the unexpected conclusion of ice on Mercury.

Observations of Mercury by ground-based or even space-based optical techniques are hampered by its close proximity to the sun (the greatest separation from the sun is about 28°). Spacecraft observations are difficult because of Mercury's depth in the sun's gravity well. Radar and radio methods (4, 5) have played an important role in modern observations of Mercury because these techniques are relatively insensitive to solar constraints on observations. For example, Mercury's rotation was believed to be synchronously locked to the

sun at an 88-day period (6) until continuous wave radar observations by Pettengill and Dyce (7) provided the first correct measurement of the period at 59 days. The topography of the equatorial regions of Mercury has been well studied with conventional delay-Doppler radar techniques (5, 8). In visible light, the only images at useful resolutions were obtained by Mariner-10 in 1974–1975, which mapped roughly half of the planet (9). The geological interpretations of these images were summarized as "an extraordinary similarity to the surface of the moon" (9). However, in contrast with the moon, Mercury has a relatively strong magnetic field (10) and a surface gravity similar to that of Mars. Mercury's surface is left as the most poorly mapped of the terrestrial planets with completion of the radar mapping of the Venus surface by Magellan. Mercury has been characterized as an "end member" of the terrestrial planets by Chapman (6) because of its location, size, and density. Comparative planetology of the terrestrial planets is seriously compromised by the absence of a complete sample of Mercury.

To obtain additional data on the unmapped portion of Mercury's surface, we conducted radar observations on 8 August and again on 23 August 1991. Our system consisted of the National Aeronautics and Space Administration/Jet Propulsion Laboratory (NASA/JPL) Goldstone 70-m transmitter and the Very Large Array (VLA) at the National Radio Astronomy Observatory in Socorro, New Mexico, as the receiving instrument. A new technique in radar

M. A. Slade, Jet Propulsion Laboratory, California Institute of Technology, Pasadena, CA 91109-8099.  
B. J. Butler and D. O. Muhleman, Division of Geological and Planetary Sciences, California Institute of Technology, Pasadena, CA 91125.

\*To whom correspondence should be addressed.

astronomy—used since 1987 to map Saturn's rings (11), Mars (12), and Venus (13) and to obtain echoes from Saturn's largest moon, Titan (14)—was used to image the full disk of Mercury on each date. This new technique of using the spatial resolution capabilities of the VLA applies aperture synthesis (15) used in radio astronomy to the received signal in a bistatic radar observation. The radar transmissions from the Goldstone 70-m antenna were essentially the same as for the earlier VLA radar observations, except that transmitted power was increased from 360 to ~460 kW and the center frequency was changed from 8.495 to 8.510 GHz.

Mercury and Venus offer ideal opportunities to apply the aperture synthesis technique (15) to planetary radar observations, because their rotation rates are sufficiently slow that integrations of several hours can be made without significant smearing of a resolution element. Thus, large rotations of the projected interferometer base lines on Mercury are achieved with excellent sampling of the spatial frequencies of the echo brightness. For the resolution on Mercury to be optimal, the observations must be performed when the VLA is in its most widely spaced configuration, called the A-array (36 km maximum spacing between antennas). The other constraint for optimal resolution is that Mercury's maximum angular size occurs at inferior conjunctions (when the planet is closest to Earth). When Mercury is observed under these conditions, the minimum fringe spacing is on the order of 100 km at the sub-Earth location on Mercury. The first such fortuitous coincidence of all these factors and the resources for a radar experiment came in August 1991.

The radar signals transmitted to Mercury were right circularly polarized (RCP), essentially monochromatic waves. These signals were programmed so that the echo received at the VLA from a nonrotating mirror surface at Mercury would be monochromatic left circularly polarized (LCP) signals centered at 8.51 GHz. In general, the VLA can process all four polarization possibilities for the correlations between antennas (16, 17) so that a full description of the polarization states of the signal can be reconstructed. These four polarization modes are designated RR\*, RL\*, LR\*, and LL\* by the VLA [see, for example, Napier *et al.* (16); see also (18)]. For these experiments with RCP transmissions, the LL\* or LCP mode of reception is known as "expected," "polarized," or "opposite sense circular" (OS). The RR\* or RCP mode is called variously "unexpected," "depolarized," or "same sense circular" (SS). We follow the usage established in Muhleman *et al.* (12), in which OS and SS are used for the circular polarization reception modes.

The first day of observations (8 August) was chosen because the hemisphere not mapped by Mariner 10 (roughly 180° to 360°) was nearly centered in longitude at ~252°. On the second day (23 August), the sub-Earth longitude of ~353° allowed

us to compare the radar returns from a portion of the planet with the photographs taken by the Mariner 10 spacecraft. On both days, the sub-Earth latitudes were far enough north for our instruments to see over the north pole and into areas thought

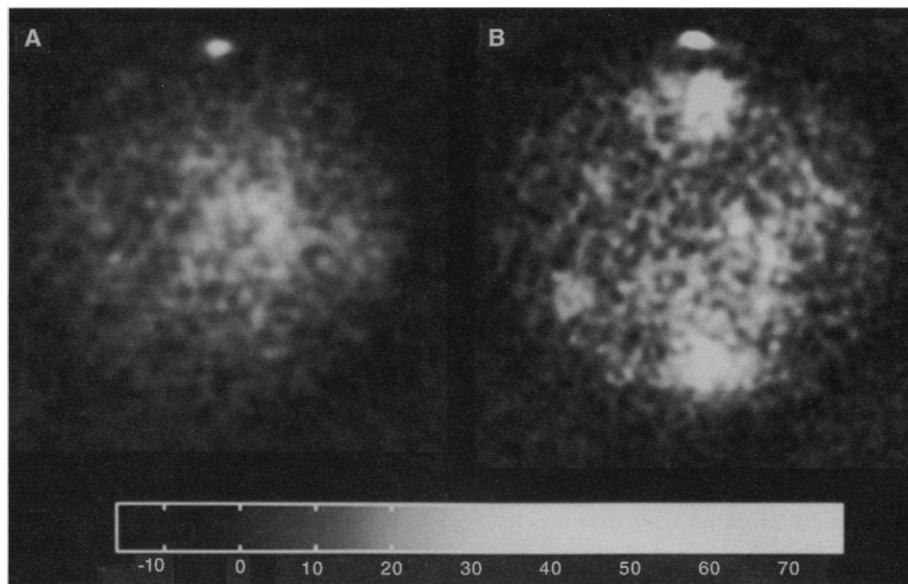


**Fig. 1.** Goldstone/VLA SS, or "depolarized," radar images of the Mercury disk for (A) 8 August 1991 and (B) 23 August 1991. North is at the top. Scale, radar reflectivity  $\times 10^{-3}$  (see Eq. 1).

**Table 1.** Mercury Goldstone/VLA experiment parameters. Latitude and longitude are the average latitude and longitude of the sub-Earth point projected on Mercury's surface; AU, astronomical units.

Date (1991)	Earth-Mercury distance (AU)	Channel bandwidth (Hz)	Number of channels	Average power (kW)	Latitude	Longitude
8 August	0.67	763	256	460	10.7	252.8
23 August	0.63	1526	128	460	11.0	353.5

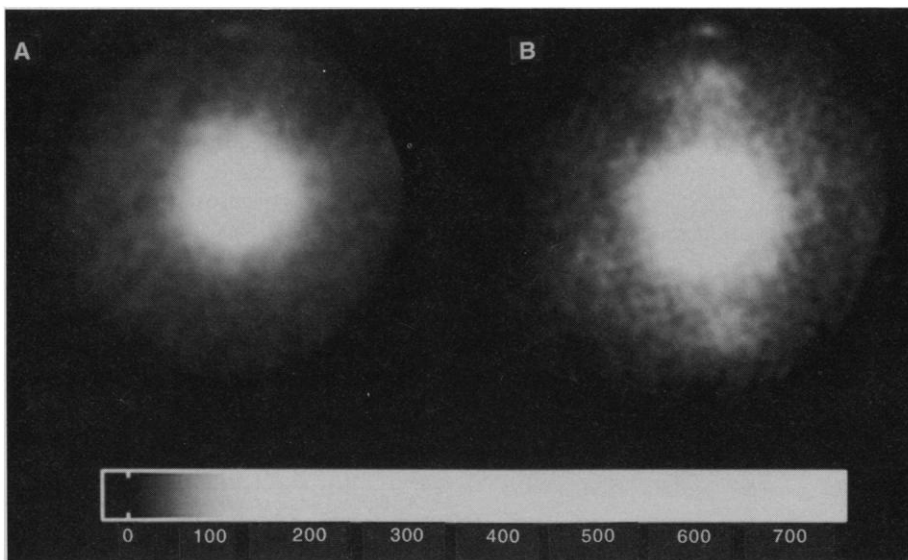


**Fig. 2.** Goldstone/VLA OS, or "polarized," radar images of the Mercury disk for (A) 8 August 1991 and (B) 23 August 1991. Scale, radar reflectivity  $\times 10^{-3}$  (see Eq. 1).

to be permanently shadowed from the sun (Table 1). On the first day, the VLA observed for 10 hours receiving OS and SS circular polarizations, with the radar illumination present for 9 hours. Calibration of the amplitudes and phases of the complex visibilities from the 325 base lines were initially derived from data on 1041+061, a quasi-stellar radio source. Absolute amplitude calibration was obtained from 1328+307, a standard VLA radio calibrator source with a flux of 5.24 Jy at our observing frequency ( $1 \text{ Jy} = 10^{-26} \text{ W m}^{-2} \text{ Hz}^{-1}$ ). The OS radar return from the first Fresnel zone around the sub-Earth point (the so-called "specular" spike) was sufficiently

strong that self-calibration (19) was possible for the OS radar visibilities. The resultant self-calibration was applied to both the SS radar and thermal continuum visibilities because this procedure removes many effects of errors in base lines and atmospheric phase fluctuations common to both receivers on each telescope. From the resulting visibilities of the central channels (of the two polarization modes), radar reflectivity maps were synthesized for the 9 hours spanned when the radar was turned on. The known synthetic antenna response (the "beam") was deconvolved with the CLEAN algorithm (20). The synthesized beam was 0.35 inch in diameter, giving a

resolution of 165 km at the subradar point for the first day (see Table 1).

The second radar synthesis mapping of Mercury was performed on 23 August 1991. The VLA was configured to record all four correlations of the two orthogonal circular polarizations (16, 17). To record all four correlations, the channel bandwidth of the observations had to be increased by a factor of 2 because of hardware constraints at the VLA. Ordinarily, this would have resulted in a penalty of  $2^{-1/2}$  in the signal-to-noise ratio because the initial bandwidth was already greater than the total Doppler spread of Mercury ( $\sim 370 \text{ Hz}$ ). However, because of good phase stability, on the second day of measurements the signal-to-noise ratio was similar to that on the first day. All calibration was done in a manner similar to that for the first day. The synthesized beam was 0.30 inch in diameter, giving a resolution of 140 km at the subradar point on the second day.

The "depolarized," or SS, images from the 2 days (Fig. 1) were converted from pixels in janskys per beam  $F_{\text{rec}}(\theta)$ , to pixels in (dimensionless) radar reflectivity  $\eta$  by division by the reference value computed from the "radar equation" (Eq. 2 below)

$$\eta(\theta) = \frac{F_{\text{rec}}(\theta)}{F_{\text{ref}}} \quad (1)$$

where  $\theta$  is the angle of incidence between the radar line of sight and the surface normal, and  $F_{\text{ref}}$  is the reference signal intensity (in janskys per beam)

$$F_{\text{ref}} \equiv \frac{P_t A_t}{4\pi \lambda^2} \frac{1}{D^2 \Delta f} \Omega_b \quad (2)$$

where  $P_t$  is the power transmitted at wavelength  $\lambda$ ,  $A_t$  is the effective area of the transmitting antenna,  $D$  is the distance to Mercury,  $\Omega_b$  is the solid angle of a beam, and  $\Delta f$  is the spectral channel bandwidth [see (12) and (14)]. The OS images (Fig. 2) were converted to radar reflectivity in a similar fashion. In the OS images, the dominant feature is the central "specular spike." A radar-bright north polar region is clearly visible in all four images (Figs. 1 and 2). The SS images have a striking resemblance to SS radar images of the Martian south residual ice cap (12).

An important measurement in this work is the pixel-by-pixel circular polarization ratio  $\mu_c$ , that results from division of the values in Fig. 1, the SS reflectivities, by the values in Fig. 2, the OS reflectivities. Maps of  $\mu_c$  (Fig. 3) were derived by the use of this division, with the result canceled if both the divisor and the dividend are not statistically different from zero in the noise of the individual maps. (In the central region of both maps, the inverse "spike" of the specular OS drives this area to zero until the

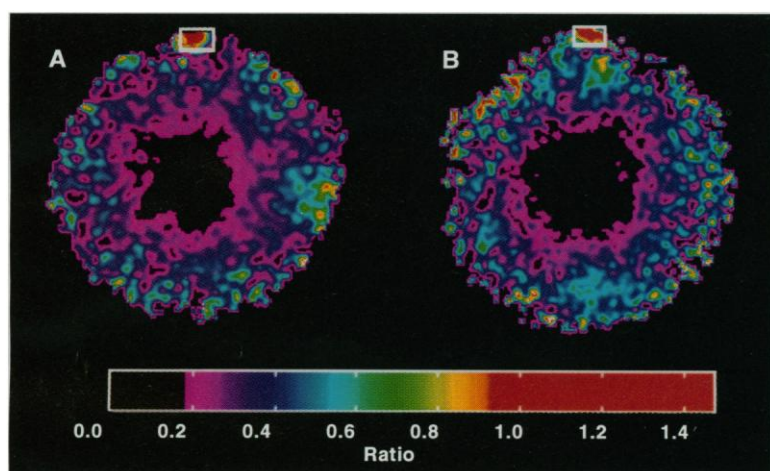


**Fig. 3.** Polarization ratios of the SS radar echo to the OS radar echo on the Mercury disk for each experiment, shown in false color; (A) 8 August 1991 and (B) 23 August 1991. The boxed areas around the pole correspond to regions in numerical form in Table 2.

**Table 2.** Polarization ratios  $\mu_c$  of SS reflectivities to OS reflectivities. The axes are row and column number of the location of the pixel relative to the pixel of the assumed north pole. Pixels are 0.1 by 0.1 arc sec in size.

x,y	-5	-4	-3	-2	-1	0	1	2	3	4	5
8 August 1991											
3											
2											
1						1.24	1.01	0.96			
0	0.97	1.19	1.39	1.47	1.41	1.24	1.12	1.02	0.83	0.52	0.35
-1	0.84	0.97	1.13	1.24	1.26	1.23	1.15	1.00	0.76	0.50	0.34
-2	0.77	0.86	1.04	1.16	1.21	1.22	1.14	0.94	0.70	0.50	0.37
-3	0.81	0.86	1.04	1.13	1.15	1.11	0.98	0.77	0.58	0.43	0.30
-4	1.06	1.06	1.18	1.17	1.05	0.85	0.67	0.52	0.38	0.27	
-5				1.23	0.95	0.67	0.56	0.50	0.34		
-6	0.45			0.94	0.78	0.63	0.63	0.61	0.41		
23 August 1991											
3			1.04	1.23	1.10	1.04	1.06	1.10			
2		0.43	0.68	1.16	1.31	1.22	1.18	1.25	1.45	1.42	0.92
1		0.55	0.71	1.04	1.24	1.23	1.24	1.32	1.45	1.35	1.04
0	0.75	0.71	0.72	0.86	1.04	1.11	1.16	1.24	1.26	1.13	1.00
-1	0.82	0.72	0.65	0.63	0.72	0.83	0.92	1.07	1.05	0.93	0.90
-2	0.75	0.55	0.53	0.59	0.65	0.67	0.66	0.84	0.86	0.74	0.66
-3	0.51	0.41	0.48	0.71	0.78	0.62			0.66	0.58	
-4		0.44	0.48	0.61	0.58					0.49	
-5		0.42	0.43	0.43						0.41	0.36
-6		0.39	0.43	0.36				0.41	0.48	0.41	

**Table 3.** Standard deviations of ratios in Table 2.

x,y	-5	-4	-3	-2	-1	0	1	2	3	4	5
<i>8 August 1991</i>											
3											
2											
1						0.57	0.48	0.51			
0	0.43	0.44	0.43	0.39	0.33	0.27	0.26	0.27	0.28	0.23	0.20
-1	0.25	0.22	0.21	0.20	0.19	0.19	0.19	0.19	0.17	0.15	0.15
-2	0.20	0.17	0.17	0.17	0.17	0.18	0.19	0.17	0.14	0.13	0.14
-3	0.26	0.21	0.22	0.20	0.20	0.21	0.21	0.18	0.15	0.13	0.13
-4	0.49	0.42	0.38	0.31	0.25	0.22	0.20	0.18	0.15	0.13	
-5				0.47	0.29	0.21	0.20	0.22	0.18		
-6	0.28			0.46	0.31	0.24	0.26	0.28	0.21		
<i>23 August 1991</i>											
3				0.34	0.29	0.22	0.20	0.24	0.36		
2		0.16	0.15	0.21	0.17	0.13	0.12	0.15	0.26	0.38	0.33
1		0.15	0.13	0.15	0.14	0.11	0.10	0.13	0.19	0.22	0.21
0	0.28	0.18	0.14	0.14	0.15	0.13	0.12	0.14	0.17	0.17	0.18
-1	0.29	0.20	0.16	0.16	0.17	0.17	0.18	0.22	0.21	0.19	0.21
-2	0.27	0.18	0.17	0.21	0.25	0.24	0.26	0.33	0.28	0.23	0.23
-3	0.21	0.16	0.18	0.25	0.29	0.24			0.26	0.21	
-4		0.16	0.18	0.21	0.20					0.18	
-5		0.14	0.16	0.16						0.16	0.13
-6		0.13	0.14	0.13					0.15	0.14	0.12

diffuse component of the OS radar returns begins to dominate at incidence angles greater than about 30°.) The boxed areas in Fig. 3 indicate regions described in more detail in Tables 2 and 3, which show the values of  $\mu_c$  and the associated errors near the north pole on both days. Table 2 lists the pixel values for each of the two days while Table 3 gives the  $1\sigma$  errors associated with the corresponding pixels. The pixel locations in the tables are given relative to the pole position defined by where the normal vector to Mercury's orbit (with the origin of the vector at Mercury's center of mass) passes through the surface. The present constraint on Mercury's pole orientation is that the pole is within about 2.5° (as seen from the center of the planet) of the orbit normal (21).

The brightest pixels in the SS images on both days (Fig. 1) are those in a region near (and including) the north pole of Mercury. A similar north polar feature was confirmed in 13-cm observations by Harmon and Slade (1) from Arecibo. While it is difficult to be definitive on the basis of just two images near the limb, we can most simply characterize the polar SS-enhanced regions in Fig. 1 as elliptical areas with axes that varied in size between the 2 days. On 8 August, the north polar bright region had a semimajor axis of ~600 km and a semiminor axis of ~175 km. The center of the ellipse was at ~88°N latitude and ~279° longitude. On 23 August, the region had a semimajor axis of ~400 km and a semiminor axis of ~150 km, with the center at ~88°N latitude and ~320° longitude. Our best resolution is normal to the line of sight, and the feature was <350 km across

in that direction on both days. Because the observations were made on 2 days and Mercury had rotated about 100° between the days, we estimate that the extent of the polar feature is <350 km across in any direction. The extent along the line of sight appears to be an artifact of the geometry near the limb, although some true ellipticity cannot be ruled out.

The values of  $\mu_c$  in Fig. 3 are the largest (that is, the brightest meaningful pixels with the greatest ratios) in the same north polar region where the largest reflectivities are found. Elsewhere in the solar system,  $\mu_c$  values as high as the 1.4 observed for this polar feature are believed to arise from coherent backscattering due to volume scattering from density fluctuations, cracks, voids, or particles embedded in ices (22, 23). Water ice is essentially transparent at our wavelength; this property results in high-order multiple scattering with little radar energy absorption. Because water apparently is supplied abundantly by impactors and outgassing from the planet, water ice is likely the material in which the volume scattering takes place (2). We also know that the optical constants for water ice and carbon dioxide ice are essentially identical at centimeter wavelengths. Therefore, we might expect that the Mercury polar feature would be very similar to the Mars south polar residual ice cap as seen by radar (12). The SS reflectivity of the Martian polar feature is roughly 70%; in contrast, the reflectivity of the north polar region on Mercury ranges between 4 and 8% at similar (nearly grazing) angles of incidence. This difference can be explained in simplest terms by a combination of (i)

the difference in the amount of surface area covered by ice; (ii) absorption, either in a thin layer covering the ice or in the ice layer itself; and (iii) the thickness of the ice. For the Mars ice cap, we know from Viking Orbiter and Mariner 9 imaging that the area covered by ice is roughly 100% of the radar-bright feature and that the ice appears quite clean (24). If the fractional surface area covered by ice on Mercury were 6 to 11% of the surface area of the feature, then the reflectivity difference would be explained.

Alternatively, a covering layer of absorbing material, which would affect the two polarizations equally, could also produce the reduced reflectivities of the Mercury polar feature. For plausible geological materials, depths of 0.5 to 1 m appear to explain the reduced reflectivity (2). An indication that an absorbing layer plays some role in the reduced reflectivity comes from the Arecibo observations (1), in which the average reflectivity of the northern feature was between 10 and 14%. At 13 cm, the radar will penetrate the layer more easily because the absorption distance in wavelengths will be smaller. However, the forward-scattering properties of the volume scatterers will also be different at 13 cm, so quantitative conclusions concerning the depth of the absorbing layer are not unique. The size of the north polar feature is similar at both wavelengths (170 by 340 km at 13 cm), indicating that the ices are many wavelengths thick at either frequency (23). The final alternative—ice layers sufficiently thinner than those on Mars to explain the lower reflectivity—is more difficult to quantify because the result depends on the nature of the scattering mechanism or mechanisms in the ice.

Water ice can exist in regions around the poles of Mercury if water molecules are placed there. Any smooth regions near the Mercury poles have been shown sufficiently cold that water ice is stable for moderately large Bond albedos (3) and any permanently shadowed regions are much colder. Ice in these shadowed regions could never be seen in reflected sunlight, by definition. Water ice is likely to be stable at the temperatures of the polar regions of Mercury on time scales longer than several hundred million years (assuming that Mercury has been trapped in its current Cassini rotational state for >1 billion years) (2, 3). We conclude that water ice appears present in a region around the north pole of Mercury. The possible sources, sinks, paths of migration, and stability of the water ice are beyond the scope of our report and have been considered in (2).

The SS image from 8 August (Fig. 1A) has a roughly circular feature of bright material about 1000 km in diameter near

the center of the disk, from about 230° to 250° longitude at a latitude of about 13°N. This feature apparently accounts for a major "spectral salient" observed by Goldstein (5) in continuous wave observations of Mercury 20 years ago. Two areas of enhanced radar echo, both about 1000 km across and near longitude 348°, were observed on 23 August and are located at 55°N and 27°S. The combined signature of these structures was detected as another major "spectral salient" in Doppler spectra observations by Goldstein (5). Our  $\mu_c$  maps in the vicinity of these structures reveal nothing striking: values of  $\sim 0.6$ , which suggest strong diffuse scattering with rough correlation to the locations of the structures. The most analogous radar counterparts to these structures (at similar angles of incidence) appear in 70-cm observations of the craters Tycho, Langenus, and Eudoxus on the moon (25). The first two of these craters also have the same appearance at 3.8 cm (26) as at 70 cm, namely, bright walls and bright interiors in both polarized and depolarized radar maps. Because these craters are known to date from late in the heavy bombardment phase of lunar cratering history, the explanation offered for their distinctive radar appearance is that the rock populations—surface or subsurface—at the appropriate size scales have not been present long enough to be degraded by lunar regolith gardening from smaller impacts (27). Thus, the observed large features on Mercury may similarly have rock populations that have not been gardened into Mercurian regolith. Alternatively, the interiors of the Mercury SS structures may be filled with fresh radar-bright lava flows. The rims of the Mercury SS structures may still be radar-bright if mass-wasting continuously renewed rubble on wavelength scales. In either case, the tentative hypothesis is that these two structures and the feature from 8 August are the result of large impacts late in the cratering history of Mercury.

Precise radar topography measurements over these features are needed. Some supporting evidence for impact origin comes from the observation that the latitudes and longitudes of the two structures from 23 August correspond well with regions where enhanced and variable sodium abundance has been previously measured in the tenuous atmosphere of Mercury (28). A similar atmospheric enhancement, but in potassium, has also been measured above the Caloris Basin (29). However, sodium and potassium enhancements also have been found above regions with no distinct radar features. The cause of the enhanced and variable atmospheric sodium emission is still under debate, but increased concentrations of sodium ions may be due simply to the geometry of convergence of the mag-

netic field lines near the magnetic poles (28). On the other hand, it may result from enhanced diffusion and degassing of sodium from within the planet through highly fractured ground in and around large impact basins (29). If this is the dominant source, then the identification of the radar-bright structures as large impact basins is further supported. Radar maps of the Caloris Basin in both polarization modes at several angles of incidence are needed to interpret these features.

The SS image from 23 August (Fig. 1B) also reveals a complex group of small radar-bright areas between longitudes 320° to 345°W. Three regions located at 330°W, 6°N, 335°W, -7°S, and 340°W, 15°N appear particularly strong. Arecibo radar altimetry (8) shows what appears to be a large crater between 325° and 330°W; its ejecta extends at least up to 10.8°N.

Nearly half of the radar images from 23 August show portions of Mercury also mapped by Mariner 10 imagery. In the SS radar echo image, areas brighter than their environs include a large region around the Kuiper crater and areas to the northwest of the Monet and Rodin craters. The crater floor of Kuiper appears slightly darker than its surroundings. Other relatively dark areas can be found, many of which occur in the interiors of circular depressions (for example, Homer and Rodin craters). Many of these large depressions contain what have been called smooth plains, most of which occur on the part of Mercury not imaged during our experiment. However, we predict that the radar reflectivity of these regions is similarly depressed because of the lack of surface roughness or volume scatterers on the scale of the radar wavelength. The OS and SS images are examined in more detail in (2). The OS images shown there are "flattened" with a Muhleman's scattering model (30) fit that removes most of the effect of the specular "spike." The SS images are also "flattened," but with a  $\cos^{1.6}$  (6) law, with the exponent of the law determined by fits to the data.

The interpretation of the polar radar features on Mercury relies on high values of  $\mu_c$  as evidence for ice, partly by analogy to other icy surfaces and partly through the theory of coherent backscattering. We hope that the observations reported here will encourage extensive investigation into the radar properties of cold icy surfaces. Passive radio observations of Mercury, in addition to radar experiments, could be performed whenever the relative orbital geometry brings the poles into their best view. Such broadband radio measurements of both poles at a variety of wavelengths could provide crucial tests for the presence of the temperatures required for water ice to be stable at the poles of Mercury.

## REFERENCES AND NOTES

1. J. K. Harmon and M. A. Slade, *Science* **258**, 640 (1992).
2. The details of the observations and a full discussion of the likelihood and stability of ice, particularly in the permanently shadowed areas of Mercury's poles, are presented in B. Butler, D. O. Muhleman, M. A. Slade, in preparation.
3. D. A. Paige, S. E. Wood, A. R. Vasavada, *Science* **258**, 643 (1992).
4. G. H. Pettengill, R. B. Dyce, D. Campbell, *Astron. J.* **72**, 330 (1967); D. Morrison, *Space Sci. Rev.* **11**, 271 (1970); R. P. Ingalls and L. P. Rainville, *Astron. J.* **77**, 185 (1972); J. N. Cuzzi, *Astrophys. J.* **189**, 577 (1974); S. Zohar and R. M. Goldstein, *Astron. J.* **79**, 85 (1974); P. E. Clark, M. A. Leake, R. F. Jurgens, in *Mercury*, F. Vilas, C. R. Chapman, M. S. Matthews, Eds. (Univ. of Arizona Press, Tucson, 1988), pp. 77–100; J. K. Harmon and D. B. Campbell, in *ibid.*, pp. 101–117.
5. R. M. Goldstein, *Science* **168**, 467 (1970); *Astron. J.* **76**, 1152 (1971).
6. C. R. Chapman [in *Mercury*, F. Vilas, C. R. Chapman, M. S. Matthews, Eds. (Univ. of Arizona Press, Tucson, 1988), pp. 1–23] has explained how the optical data were ambiguous because the data reductions had not allowed for the possibility that Mercury had rotated by more than 360° between observations. *Mercury* is an excellent summary of the state of the studies of Mercury as of 1986.
7. G. H. Pettengill and R. B. Dyce, *Nature* **206**, 1240 (1965).
8. J. K. Harmon, D. B. Campbell, D. L. Bindschadler, J. W. Head, I. I. Shapiro, *J. Geophys. Res.* **91** (no. B1), 385 (1986).
9. B. C. Murray *et al.*, *Science* **185**, 169 (1974).
10. N. F. Ness, K. W. Behannon, R. P. Lepping, Y. C. Whang, K. H. Schatten, *ibid.*, p. 151.
11. D. O. Muhleman, A. W. Grossman, R. M. Goldstein, *Bull. Am. Astron. Soc.* **19**, 882 (1987).
12. D. O. Muhleman, B. J. Butler, A. W. Grossman, M. A. Slade, *Science* **253**, 1508 (1991).
13. K. A. Tryka *et al.*, *Lunar Planet. Sci.* **22**, 1417 (1991).
14. D. O. Muhleman, A. W. Grossman, B. J. Butler, M. A. Slade, *Science* **248**, 975 (1990).
15. A. R. Thompson, J. M. Moran, G. W. Swenson, Jr., *Interferometry and Synthesis in Radio Astronomy* (Wiley, New York, 1986), pp. 48–56.
16. The hardware at the VLA and Goldstone dictate right (R) and left (L) circular polarization as our orthogonal modes of reception. The four quantities that can be formed are  $R\otimes R^*$ ,  $R\otimes L^*$ ,  $L\otimes R^*$ , and  $L\otimes L^*$ , where  $\otimes$  means correlation and  $*$  means complex conjugation. One common way of representing the four independent quantities are the so-called "Stokes parameters." See P. J. Napier, A. R. Thompson, R. D. Ekers, *Proc. IEEE* **71** (no. 11), 1295 (1983).
17. See B. G. Clark, in *Synthesis Imaging in Radio Astronomy*, R. A. Perley, F. R. Schwab, A. H. Bridle, Eds. (Astronomical Society of the Pacific, San Francisco, 1989), pp. 9–10.
18. A. R. Thompson, J. M. Moran, G. W. Swenson, Jr., *Interferometry and Synthesis in Radio Astronomy* (Wiley, New York, 1986), pp. 97–106.
19. Self-calibration is a least-squares solution for the best set of antenna-based amplitudes and phases as a function of time with the use of redundant information that exists for a simple source. This procedure is closely related to "closure phase" and "adaptive optics." See, for example, E. B. Fomalont and R. A. Perley, in (17), pp. 83–114.
20. J. A. Högbom, in *Image Formation from Coherence Functions in Astronomy*, C. van Schooneveld, Ed. (Reidel, Dordrecht, the Netherlands, 1983), pp. 237–239. See also T. J. Cornwell, *Astron. Astrophys.* **121**, 281 (1983).
21. The most accurate determination of Mercury's spin vector orientation until recently was that of K. P. Klaassen [*Icarus* **28**, 469 (1976)]. This determination is consistent with Mercury in the 3/2 resonance in the Cassini state 1. S. J. Peale [*Astron. J.* **74**, 483 (1969)] argues that the obliquity of Mer-

cury is nearly zero. In (1), Harmon and Slade argue that the Arecibo observations further constrain the pole direction fortuitously along the direction of greatest uncertainty in Klaasen's 50% error ellipse (but not reducing the 2.5° error in the orthogonal direction).

22. B. Hapke, *Icarus* **88**, 407 (1990); \_\_\_\_\_ and D. Blewitt, *Nature* **352**, 46 (1991).
23. K. J. Peters, *Phys. Rev. B* **46** (no. 2), 801 (1992).
24. Unit 1 in figure 1 of K. E. Herkenhoff and B. C. Murray, *J. Geophys. Res.* **95**, 1343 (1990).
25. T. W. Thompson, *Moon* **10**, 51 (1974).
26. S. H. Zisk, G. H. Pettengill, G. W. Catuna, *ibid.*, p. 17.
27. T. W. Thompson, S. H. Zisk, R. W. Shorthill, P. H. Schultz, J. A. Cutts, *Icarus* **46**, 201 (1981).
28. A. E. Potter and T. H. Morgan, *Science* **248**, 835 (1990); see also R. M. Killen, A. E. Potter, T. H. Morgan, *Icarus* **85**, 145 (1990).
29. A. L. Sprague, R. W. H. Kozlowski, D. M. Hunten, *Science* **249**, 1140 (1990). See also A. L. Sprague, *Icarus* **84**, 93 (1990); R. M. Killen, A. E. Potter, T. H. Morgan, *Science* **252**, 974 (1991); A.

- L. Sprague, R. W. H. Kozlowski, D. M. Hunten, *ibid.*, p. 975.
30. D. O. Muhleman, *Astron. J.* **69**, 34 (1964).
31. We thank the observing staff at the VLA and the Radio Astronomy and Radar Group at Goldstone for the attention and care in performing the experiments. In particular we thank K. Sowinski and W. M. Goss for their help in various aspects of these experiments. R. F. Jurgens, E. M. Standish, Jr., and D. K. Yeomans provided assistance with radar operations and ephemerides. We also thank D. A. Paige, S. E. Wood, A. R. Vasavada, and J. K. Harmon for discussions of their results before publication. Part of the research described above was carried out at the Jet Propulsion Laboratory, California Institute of Technology, under a contract with the National Aeronautics and Space Administration. The Caltech work was supported under NASA grant NAGW 1499. Contribution number 5158 from the Division of Geological and Planetary Sciences, Caltech.

3 June 1992; accepted 4 August 1992

## Radar Mapping of Mercury: Full-Disk Images and Polar Anomalies

J. K. Harmon and M. A. Slade

A random-code technique has been used at Arecibo to obtain delay-Doppler radar images of the full disk of Mercury. Anomalous bright features were found at the north and south poles. The north polar feature is oblong (4° by 8°) and offset from the pole. The smaller south polar feature is mostly confined to the floor of the crater Chao Meng-Fu. The polar locations and radar properties of these features indicate that they may be produced by volume scattering in ice. The images also reveal a variety of more subdued reflectivity features ranging in size from hundreds to thousands of kilometers; some of these appear to have an impact origin.

Radar reflectivity mapping of Mercury has been limited in the past to delay-Doppler imaging of the polarized echo (1) in the near-subradar region (2, 3). Full-disk imaging and depolarized imaging of the planet have been deterred by problems such as low echo strength and "overspreading" (4). Recent advances have been made in overcoming these limitations with the use of synthesis mapping between Goldstone and the Very Large Array (VLA) (5) and random-code delay-Doppler mapping at Arecibo. The new full-disk radar images obtained at these facilities have revealed several interesting radar features of Mercury, most notably the anomalous bright spots at the north and south poles. Here we present some of the new Arecibo results.

The mapping observations were made on a total of 28 dates during three separate periods near inferior conjunction: 28 March to 21 April 1991, 31 July to 29 August 1991, and 14 to 29 March 1992. The subradar track during the spring 1991 observations went from (in planetocentric, or

longitude/latitude, coordinates) 285°W, 5.3°S to 79°W, 3.6°S. For the summer 1991 observations the track went from 205°W, 9.2°N to 33°W, 9.5°N and reached a northernmost latitude of 11.6°N. Following the success of the 1991 observations, the March 1992 dates were added to give a better view of the south polar anomaly; the track for these observations went from 301°W, 7.1°S to 40°W, 7.4°S.

The observations were made with the Arecibo S-band ( $\lambda = 12.6$  cm) radar transmitting a 420-kW, circularly polarized wave. The transmitted wave was modulated by a nonrepeating binary phase code with a 100- $\mu$ s baud. The received signal for each orthogonal circular polarization was filtered, sampled, and processed in precisely the same way as for recent random-code mapping observations of Mars (6) except that a longer Fourier transform (8192 elements) was used to achieve a Doppler resolution of 1.22 Hz. The random-code method works on the principle that, by using a nonrepeating code, one can turn what would otherwise be a confusing aliasing of the overspread echo into an additive white-noise clutter (7). This clutter component contributes less than 15% of the

total noise background for the depolarized echo.

Each day's data were reduced to a single delay-Doppler array formed from the sum of one to three observing runs; each run had an integration time of 9 to 13 min. After estimating and subtracting a noise base line, we constructed a radar reflectivity map (image) from the delay-Doppler array. The mapping was done by construction of a 512 by 512 square array of pixels circumscribing the projected disk of Mercury. A mapping from delay-Doppler to Cartesian coordinates was done and a value representing the radar reflectivity (cross section per unit projected area) was assigned to each pixel. The image was then smoothed to an effective resolution of 5 by 3 pixels to reduce noise. Radar images made with this technique have a north-south ambiguity about the Doppler equator. We have been able to resolve the ambiguity for most of the prominent reflectivity features by comparing images obtained at different aspects. The spurious component of any given ambiguous feature pair can be identified because its mapped planetocentric position changes with aspect while the true feature remains fixed. Even small changes in subradar latitude can suffice to resolve some mapping ambiguities by eye.

Figures 1 and 2 show two sets of depolarized images obtained at northern and southern latitudes, respectively. The images are dominated by a pair of mid-latitude bright patches in the north and south at about 350°W longitude. These features are located in the hemisphere (190° to 10°W) that was not imaged by Mariner 10. The northern patch is centered at 345°W, 55°N, and the southern patch is at 348°W, 30°S. Unfortunately, the position of the Doppler equator in Fig. 1 is such that the northern and southern features are largely folded over each other (although closer inspection reveals the true location of the brightest spot in the northern feature). The two features separate out in the more southerly images (Fig. 2); the southern feature dominates, whereas the northern feature appears only as a faint patch in the far north (Fig. 2B). This change in the relative brightness of the two features is apparently an incidence-angle effect. These two features together account for one of the two depolarized enhancements seen by Goldstein (8) in continuous-wave Doppler spectra. The large equatorial bright area east of 270°W in Fig. 1A probably corresponds to Goldstein's other depolarized enhancement. Both of the 350°W mid-latitude features have reflectivities of about 0.020, which corresponds to a fivefold enhancement over the planet average. Such reflectivities and enhancement factors are reminiscent of depolarized bright spots on the

J. K. Harmon, National Astronomy and Ionosphere Center, Arecibo, PR 00613.  
M. A. Slade, Jet Propulsion Laboratory, California Institute of Technology, Pasadena, CA 91109.